

Experimental Investigation of Vortex Generators on a Low-Boom Supersonic Inlet

Manan A. Vyas¹, Stefanie M. Hirt², Rodrick V. Chima³ and David O. Davis⁴
NASA Glenn Research Center, Cleveland, OH, 44135

Thomas R. Wayman⁵
Gulfstream Aerospace Corporation, Savannah, GA, 31402

Vortex generators (VGs) were experimentally investigated on a single-stream Low-Boom Supersonic Inlet in the 8x6 foot Supersonic Wind Tunnel at the NASA Glenn Research Center. Four upstream micro-VG and six downstream VG configurations were designed and tested for the purpose of this work. The objectives of the test were to evaluate the effects of the upstream micro-VGs on the normal shock stability, evaluate effects of the downstream VGs on reducing the boundary-layer thickness, and determine overall inlet performance. Results are presented in terms of total pressure recovery, flow distortion, boundary-layer velocity profiles, sound pressure levels, and dynamic spectra. The results showed a marginal decrease in the total pressure recovery for all VG configurations. The upstream micro-VG did not have a significant effect on the normal shock stability. And the downstream VGs accounted for the majority of improvement in boundary-layer thickness.

Nomenclature

AOA	=	angle of attack
c	=	vortex generator chord length
c_x	=	vortex generator axial length
H_i	=	incompressible shape factor
h	=	vortex generator height
M	=	Mach number
\dot{m}	=	tunnel mass flow rate
\dot{m}_{AIP}	=	mass flow rate at aerodynamic interface plane
N	=	number of vortex generators
P_∞	=	tunnel freestream pressure
P_{AIP}	=	mean total pressure at aerodynamic interface plane
P_{60}	=	mean total pressure in 60° sector
P_i	=	mean total pressure in a ring of total pressure probes
r_{cowl}	=	cowl radius
s	=	vortex generator spacing
U_{local}	=	x velocity
U_∞	=	freestream velocity
ρ_∞	=	freestream density
α	=	vortex generator half angle

¹ Aerospace Engineer, Inlet and Nozzle Branch, MS 5-12, and AIAA Member.

² Aerospace Engineer, Inlet and Nozzle Branch, MS 5-12, and AIAA Senior Member.

³ Aerospace Engineer, Inlet and Nozzle Branch, MS 5-12, and AIAA Associate Fellow.

⁴ Aerospace Engineer, Inlet and Nozzle Branch, MS 5-12, and AIAA Senior Member.

⁵ Aero/Performance Specialist, Supersonic Technology Department, MS R-07, and AIAA Associate Fellow.

I. Introduction

Flow control devices for supersonic inlets have made significant advancements in recent years. They are considered for use in supersonic inlets to deal with shock boundary-layer interactions (SBLIs) which result in flow separation, shock losses and non-uniform flow at the engine Aerodynamic Interface Plane (AIP). SBLIs can also cause unsteady pressure loads and surface heat flux. Addressing these issues is of great importance for the future development of supersonic inlets as they affect engine performance.

Traditionally, bleed is used to reduce the fore-mentioned effects of SBLIs. Separated low-momentum flow at the wall is removed from the inlet before it reaches the AIP through a bleed hole pattern placed fore and aft of the shock location. However, to account for such flow removal the inlet needs to be sized larger to provide the same amount of mass flow to the engine. The consequences of a large inlet are additional drag and weight penalties which reduce the overall propulsion system efficiency. Moreover, bleed systems are complex and difficult to maintain. Thus, there is a need for alternative flow control mechanisms which will help advance the inlet technology to meet the future needs of supersonic and hypersonic propulsion systems.

Researchers in industry and academia have investigated other strategies of flow control such as micro-jets¹, plasma actuation², micro-ramps³, vanes⁴, and hybrid flow control⁵. Of these, ramps and vanes are of particular interest due to their simplicity. Each ramp and pair of vanes create a vortex pair that can be used to energize the boundary layer, thus they can also be referred to as vortex generators (VGs).

VGs are a simple approach to reduce the shock induced boundary-layer separation or thickening and associated pressure loss without increasing the size of the inlet or adding significant weight. They are passive flow control devices which are easy to manufacture, require minimal maintenance, and are straightforward to integrate in an inlet design in contrast to bleed.

VGs have been successfully used in the past for subsonic diffusers to improve the boundary-layer through high turning angles. Traditional VGs are typically the height of the boundary-layer thickness. However, micro-VG heights are on the order of 25%-40% of the boundary-layer thickness. A ramp-type VG generates a pair of counter-rotating vortices that transfer the high-momentum flow from the boundary-layer edge to the flow near the wall. A vane-type VG performs similarly but a pair of them is needed to generate the same counter-rotating vortices. Previous small scale experimental efforts⁶ have shown up to 40% improvement in separated flow thickness can be made with an optimized VG design. These potential advantages make them an attractive candidate for the bleedless Low-Boom Supersonic Inlet (LBSI) investigated in the 8x6 foot Supersonic Wind Tunnel (SWT) at NASA Glenn Research Center (GRC).

The LBSI is a relaxed external compression single-stream inlet designed to decrease the cowl lip angle which allows for a near constant external cowl radius. This, combined with low spillage on-design, minimizes the external pressure rise and thus the sonic boom profile. However, to achieve the small flow angle at the cowl, additional turning is required on the centerbody surface, which results in a large hub side boundary layer. The large boundary layer causes flow distortion and non-uniformity at the engine aerodynamic interface plane (AIP). To reduce the boundary-layer thickness, four micro-VG configurations upstream of the shock and six VG configurations downstream of the shock were experimentally investigated.

The objective of this work was to investigate the effects of the:

- Upstream micro-VGs on the normal shock stability and resulting boundary-layer thickening
- Downstream VGs on the hub side boundary layer and resulting reduction in flow distortion, which aids flow non-uniformity and the overall inlet performance.

II. Experimental Setup

A. 8x6 foot Supersonic Wind Tunnel

The 8x6 foot Supersonic Wind Tunnel (SWT) is a dual mode facility with an ability to operate in an aerodynamic closed-loop cycle as well as a propulsion open-loop cycle. The tunnel test section is 8 ft. high by 6 ft. wide and 23.5 ft. long, with test section walls that are perforated to allow for cancellation of wall reflected disturbances. Figure 1 shows the single-stream inlet and perforated tunnel walls in the test section. A stainless steel flex-wall nozzle located upstream of the test section is used to accelerate flow up to Mach 2.0. The tunnel operation spans subsonic, transonic and supersonic range and has ability to throttle from Mach 0.25 to 2.0.

Airflow to the tunnel is provided by a seven-stage motor-driven compressor located in the 8x6 foot SWT complex. The air flows through a dryer and cooler which allows for continuous operations in excess of six hours. It has a stagnation pressure range of 15.3 to 25 psia and a temperature range of 520 to 700° R.

The LBSI assembly was mounted on the tunnel bottom wall with a moveable strut which allowed changing the inlet angle of attack.



Figure 1: Single-stream inlet in the 8x6 ft. SWT test section

B. Single-Stream Low-Boom Supersonic Inlet

The experimental investigation included a dual-stream and a single-stream LBSI; however, the results presented in this paper are limited to the single-stream inlet. The dual-stream LBSI is discussed at length in References 6 and 7.

The 1:4.86 scale single-stream inlet was designed and fabricated with a goal of demonstrating the bleedless low-boom relaxed external compression concept proposed by the researchers at Gulfstream Aerospace Corporation^{8,9}. It was designed for a Mach number of 1.7. The cut-away in Fig. 2 shows the zero cowl lip angle and a low external cowl angle, which coupled with low spillage on-design minimizes external overpressures that would contribute to aircraft sonic boom. However, the low cowl angle increases flow angles at the hub in the diffuser. This causes an increase in the hub boundary-layer thickness which results in non-uniform and distorted flow at AIP. Micro-VGs upstream of the normal shock and VGs downstream of the shock were incorporated in the centerbody design, see Fig. 3, to control the boundary-layer thickening.

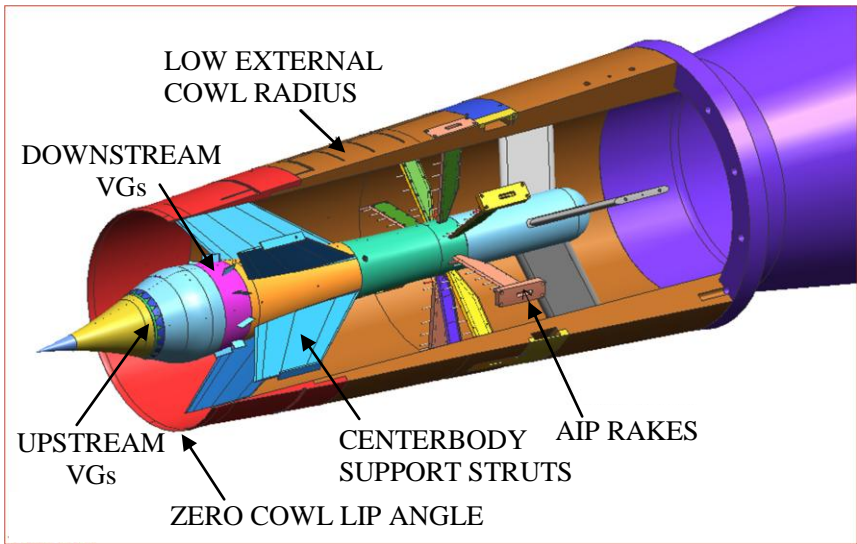


Figure 2: Single-stream inlet cut-away

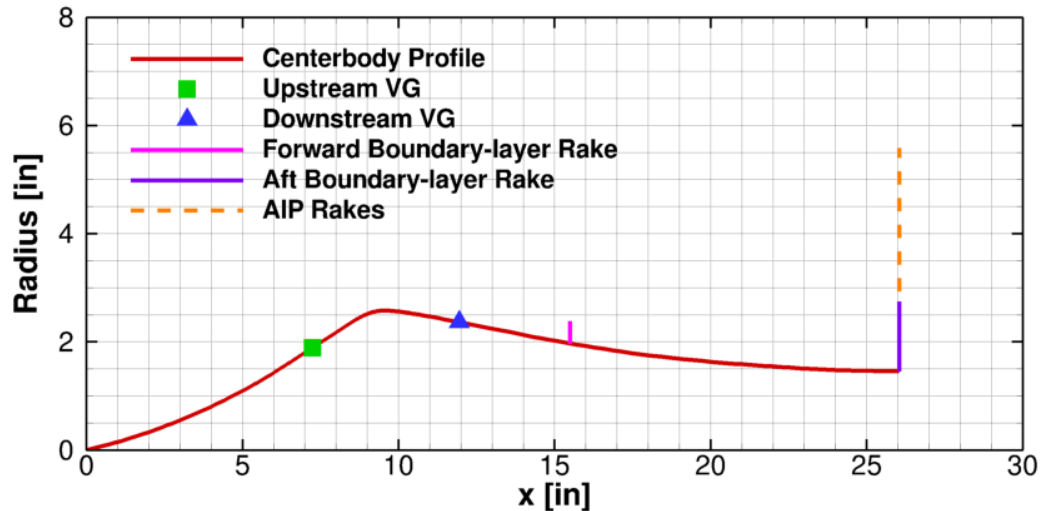


Figure 3: Inlet centerbody profile and key stations

The inlet was attached to a 16 inch cold pipe and a conical mass flow plug. The mass flow plug was opened and closed to throttle the inlet. The inlet was tested at nominal Mach numbers of 0.5, 1.4, 1.5, 1.6, 1.7, and 1.8. The angle of attack was varied from -2.0° to 5.0° with 1° increments. At each Mach number and angle of attack, the mass flow plug was translated to obtain a total pressure recovery curve, which is also known as a *cane curve*. The cane curve helps identify the inlet operational limit. The most important location on that curve is the design point, which refers to the mass flow ratio at which near maximum total pressure recovery is obtained. The other significant marker is the onset of buzz, which refers to the mass flow ratio at which the inlet shock system becomes unstable. This unstable shock system shows an oscillatory behavior. The buzz cycle starts with high-frequency, low-amplitude localized normal shock oscillations and transforms into large amplitude oscillations of the entire inlet shock system. A detail explanation of the buzz flow physics is described in References 10 and 11.

C. Vortex Generators

A total of four ramp-type micro-VGs were designed for placement upstream of the normal shock on the compression spike. These micro-VGs were intended to reduce the shock boundary-layer interactions (SBLIs) and improve the normal shock stability. Downstream VGs were designed with a purpose of reducing the boundary-layer thickness and flow distortion. A total of six vane-, plow-, and ramp-type VGs were designed for downstream placement. Upstream and downstream VG geometries are shown in Figs. 4 and 5. The VG geometry parameters are listed in Table 1.

Figure 4 depicts the ramp- and plow-type VGs and geometry parameters: inter-ramp spacing (s), ramp height (h) and chord length (c). The vortex generator half angle, α was kept constant at 24° . A plow-type VG is identical to a ramp-type VG but it is oriented so that the vertex of the VG triangle is upstream and facing the airflow. Figure 5-a shows split ramp-type VG geometry. Depending on the geometry parameters, the total number (N) of VGs was increased or decreased to cover the full circumference of the centerbody. The ramp-type VGs were designed to produce an upwash vortex pair while the plow-type VGs were designed to produce a downwash vortex pair.

The large ramp- and plow-type downstream VGs (D4R and D3P) were circumferentially aligned so that one ramp was centered between consecutive centerbody support struts, while for small ramp-type downstream VG (D6R), two ramps were centered between consecutive centerbody support struts.

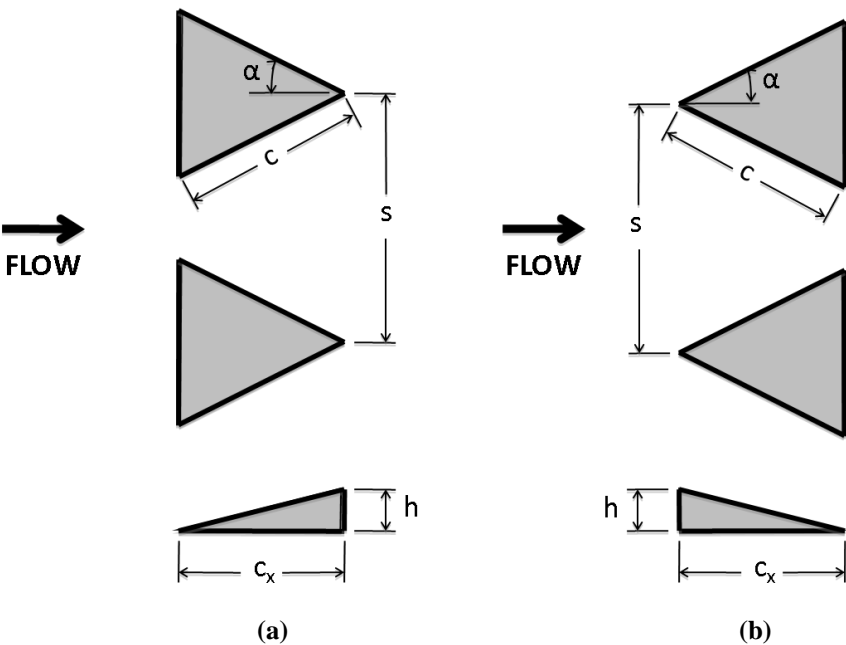


Figure 4: VG geometry parameters shown for (a) Ramp-type and (b) Flow-type

Vane-type VGs produce one vortex each, thus to produce a pair of counter-rotating vortices two vanes are placed facing each other. Placing the pressure side towards each other produces an upwash vortex pair while placing the suction sides towards each other produces a downwash vortex pair. The vanes were modeled after a half NACA 0012 airfoil which results in a vortex developing from the suction side of the vane. Figure 5-b shows three consecutive vanes with geometry parameters. They alternate with an angle of attack of either -16° or 16° with respect to the flow direction.

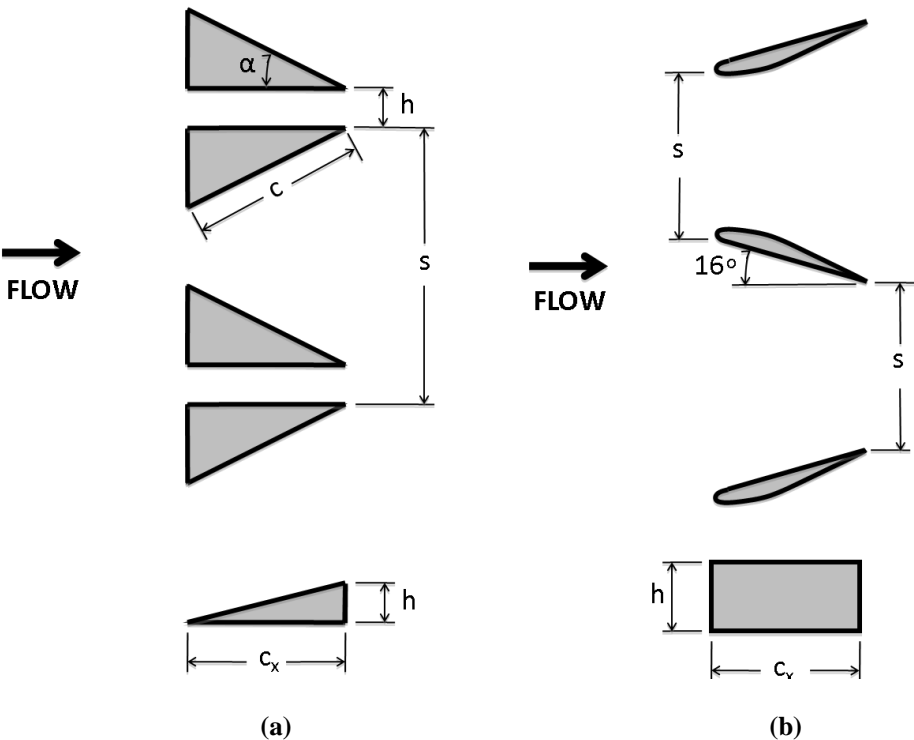


Figure 5: VG geometry parameters shown for (a) Split ramp-type and (b) Vane-type

The large vane-type downstream VGs (D1V and D2V) were circumferentially aligned so that two vanes were centered between consecutive centerbody support struts, while for small vane-type downstream VG (D5V), four vanes were centered between consecutive centerbody support struts.

Table 1 shows a list of all upstream micro-VGs and downstream VGs with parameters of interest. Specific VG configurations will be denoted using the abbreviation (e.g. U1R) in the table. For example, a case with the upstream ramp-type VG U1R and downstream vane-type VG D1V will be referred as U1R-D1V. The VG configuration **U0-D0** means no VG, which is also the baseline case.

Table 1: Vortex Generator Design Parameters

Type	Name	Spacing, s [in]	Height, h [in]	Chord, c [in]	Number, N [Total (Pair)]
Upstream micro-VGs					
Ramp	U1R	0.549	0.075	0.338	20
Ramp	U2R	0.283	0.038	0.171	40
Split Ramp	U3SR	0.733	0.075	0.338	15
Split Ramp	U4SR	0.377	0.038	0.171	30
Downstream VGs					
Vane (Upwash)	D1V (Large)	1.181	0.400	1.000	10 (5)
Vane (Downwash)	D2V (Large)	1.181	0.400	1.000	10 (5)
Plow	D3P (Large)	3.104	0.400	1.052	5
Ramp	D4R (Large)	3.054	0.400	1.052	5
Vane	D5V (Small)	0.565	0.250	0.621	20 (10)
Ramp	D6R (Small)	3.054	0.250	0.657	10

D. Instrumentation and Data Systems

The AIP distortion, total pressure recovery, sound pressure level, and dynamic pressure transducer spectra were used to evaluate the effects of upstream and downstream VGs on the boundary-layer thickness and overall inlet performance. The flow distortion was calculated based on 40 total pressure probes. These probes were installed to conform to the SAE ARP 1420 standard¹² for inlet distortion measurement. These probes were set into eight rakes with five total pressure probes spaced 45° apart circumferentially. An additional total pressure probe was added to the rakes at 45°, 135°, 225°, and 315° at the hub for better resolution of the hub side boundary layer. Inlet dynamic conditions were measured by mounting a dynamic pressure transducer on each of the eight rakes; mounted close to the hub on the rakes located at 0°, 90°, 180°, and 270° and mounted close to the cowl on the rakes located at 45°, 135°, 225°, and 315°. Figure 6 shows the AIP probe layout. The dynamic pressure transducers are marked in red dots, one each along eight AIP rakes.

A forward boundary-layer rake with eight total pressure probes was placed on the centerbody just aft of the downstream VGs. This rake was located 144° counter-clockwise from model top-dead center (Fig. 6). This will be referred to as the *forward boundary-layer rake*. Another boundary-layer rake with 14 total pressure probes was placed on the centerbody along with the AIP rakes. This rake was located 202.5° counter-clockwise from model top-dead center; and will be referred to as the *aft boundary-layer rake*. This rake is shown in Fig. 6. The axial position of forward and aft boundary-layer rakes relative to the upstream micro-VGs and downstream VGs is shown in Fig. 3. The forward boundary-layer rake, aft boundary-layer rake and the AIP rakes were used to evaluate the upstream and downstream VG effects on the boundary-layer thickness and the inlet performance.

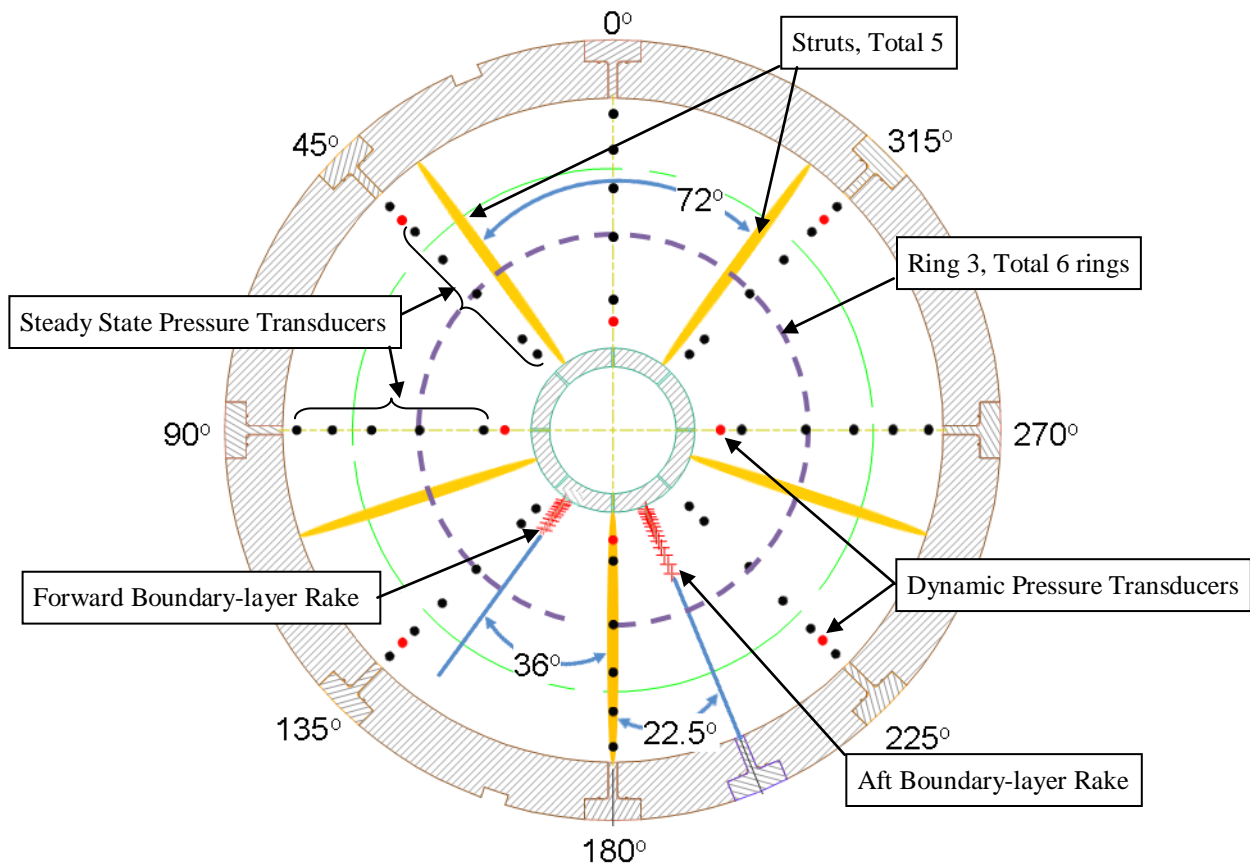


Figure 6: Circumferential layout of the AIP, boundary-layer rakes and struts (looking into the inlet)

III. Results

A. Baseline Case

The baseline single-stream LBSI did not use VGs (U0-D0). The following discussion focuses on the nominal design Mach 1.7 at three angles of attack (-2.0, 0.0, and 5.0 degrees). At each Mach number and angle of attack, the mass flow plug position was varied to obtain a total pressure recovery curve. The recovery was calculated using the 40 AIP total pressure probes. As expected, the inlet produced peak recovery at 0° angle of attack, shown in Fig. 7. The lowest peak recovery was obtained for 5° angle of attack. As the inlet was throttled and the mass flow decreased, the recovery dropped, which eventually led to the onset of buzz. Surprisingly, the total pressure recovery at buzz is the same as the normal shock recovery at Mach 1.7.

The mass flow ratio (MFR) is defined in Eq. 1, where the mass flow at the AIP is divided by the theoretical mass flow captured at the cowl lip.

$$MFR = \frac{\dot{m}_{AIP}}{\rho_{\infty} U_{\infty} \pi r_{cowl}^2} \quad (1)$$

Figure 8 shows the DC60 flow distortion coefficient for the baseline case. Like the total pressure recovery, it was calculated using the 40 AIP total pressure probes. The DC60 flow distortion coefficient is defined in Eq. (2), where P_{AIP} is the mean total pressure at the AIP and P_{60} is the mean total pressure of the 60° sector which shows the most deviation from P_{AIP} . A detailed explanation on the flow distortion coefficient is given in Reference 10. The flow distortion coefficient is a tool that helps identify flow non-uniformity at the AIP.

$$DC(60) = \frac{P_{AIP} - P_{60}}{P_{AIP}} \quad (2)$$

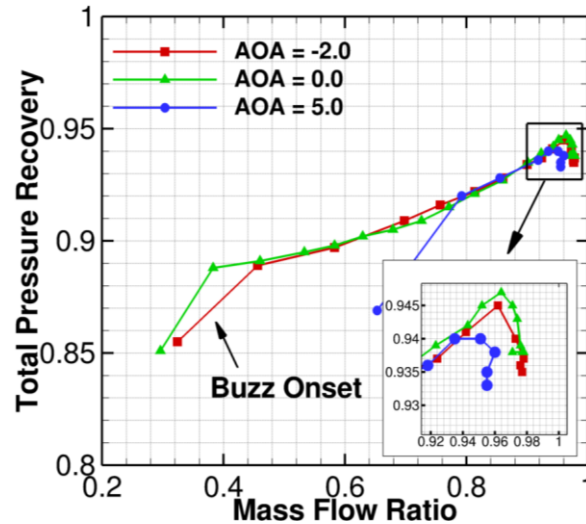


Figure 7: Baseline total pressure recovery

For all cases, the 60° sector, centered about the bottom dead center, produced the most deviation from P_{AIP} , as the AIP rake at 180° (bottom dead center) is just downstream from a centerbody support strut. Figure 6 shows the circumferential location of the struts and the AIP rakes. Figure 2 shows the axial location of the AIP rake relative to the strut location. The remaining struts should exhibit similar flow distortion behavior, but the circumferential layout of the AIP rakes did not allow for measuring this effect.

The 5° angle of attack produced the highest distortion levels. The distortion levels for 0° and -2° were quite similar. However in the expected operational range where the mass flow ratio varies from 0.8 to 1.0, the 0° angle of attack produced marginally higher distortion coefficient. At lower mass flow ratios the trend changes and 0° angle of attack produced the lowest distortion levels. At negative angle of attack, the air flow through the lower half of the inlet decreases, which results in a slightly lower distortion coefficient at high mass flow ratio.

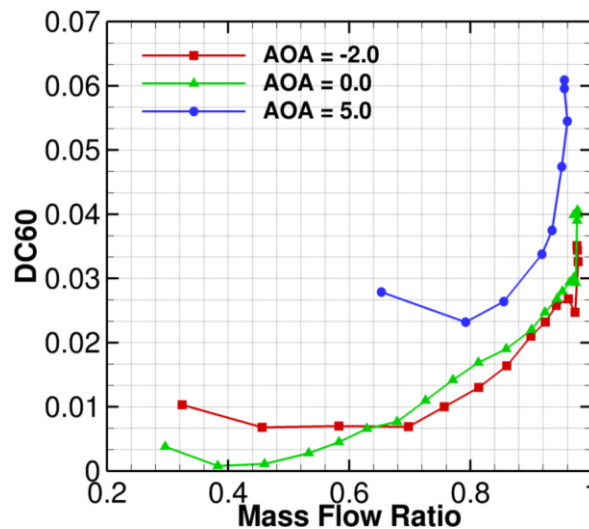


Figure 8: Baseline flow distortion coefficient

The ring-average radial distortion profile at the AIP was also calculated using the 40 AIP total pressure probes. The ring-average radial distortion is defined in Eq. 3, where P_{AIP} is the mean total pressure at the AIP and P_i is the mean total pressure of an individual ring (example of a ring is shown in Fig. 6). The ring-average radial distortion is explained at length in Reference 12.

$$\text{Radial Distortion} = \frac{P_{AIP} - P_i}{P_{AIP}} \quad (3)$$

Figure 9 shows a comparison for the baseline case at the design point in which the ring-average radial distortion coefficient is plotted versus the radial distance from centerbody. The distortion level on the hub side showed the largest change with an increase in angle of attack. Surprisingly, the distortion reduced at the hub for -2° and 5° angles of attack. The negative distortion values indicate that the ring average pressure was higher than the face average pressure.

Although, the focus of this work was the hub side boundary layer, it was also interesting to see the flow distortion effects on the tip side. The large flow distortion along the cowl surface is due to the shock impingement on the cowl lip and resulting boundary-layer thickening. An improvement to this non-uniformity was not the purpose of this work.

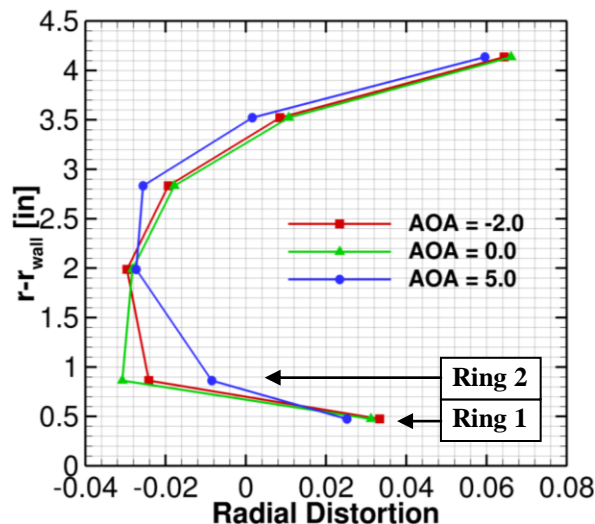


Figure 9: Baseline ring-average radial distortion coefficient profile at design point

Figure 10 shows the ring-average radial distortion coefficient for the six rings of total pressure probes which constitute the AIP rakes. The ring distortion versus mass flow ratio plot reveals the change in the distortion within each concentric ring. The rings of special interest are those close to the hub, rings 1 and 2, which quantify the effects of hub side boundary-layer thickening as the inlet is throttled.

It is evident that rings 1 and 2 show radial distortion levels with a high magnitude of change as the inlet is throttled. The 0° angle of attack produces the highest radial distortion levels. The lowest mass flow ratios represent the distortion after onset of buzz, thus a large change in the distortion coefficient results. However, the level of distortion cannot be measured accurately for the buzz condition as half of the probes on ring 1 and all on ring 2 were steady state measurements and were not able to capture the high frequency dynamic pressure changes. The distortion level at the design point is approximately 0.03.

Rings 3 and 4 showed a lower level of distortion and reduced magnitude of change which implied that the flow was uniform. The distortion levels at the design point were approximately 0.02. Ring 5 showed a moderate increase in the overall distortion levels but it had the lowest distortion at the design point. The highest distortion level was found in ring 6, which was closest to the tip side, where distortion levels exceeded 0.06.

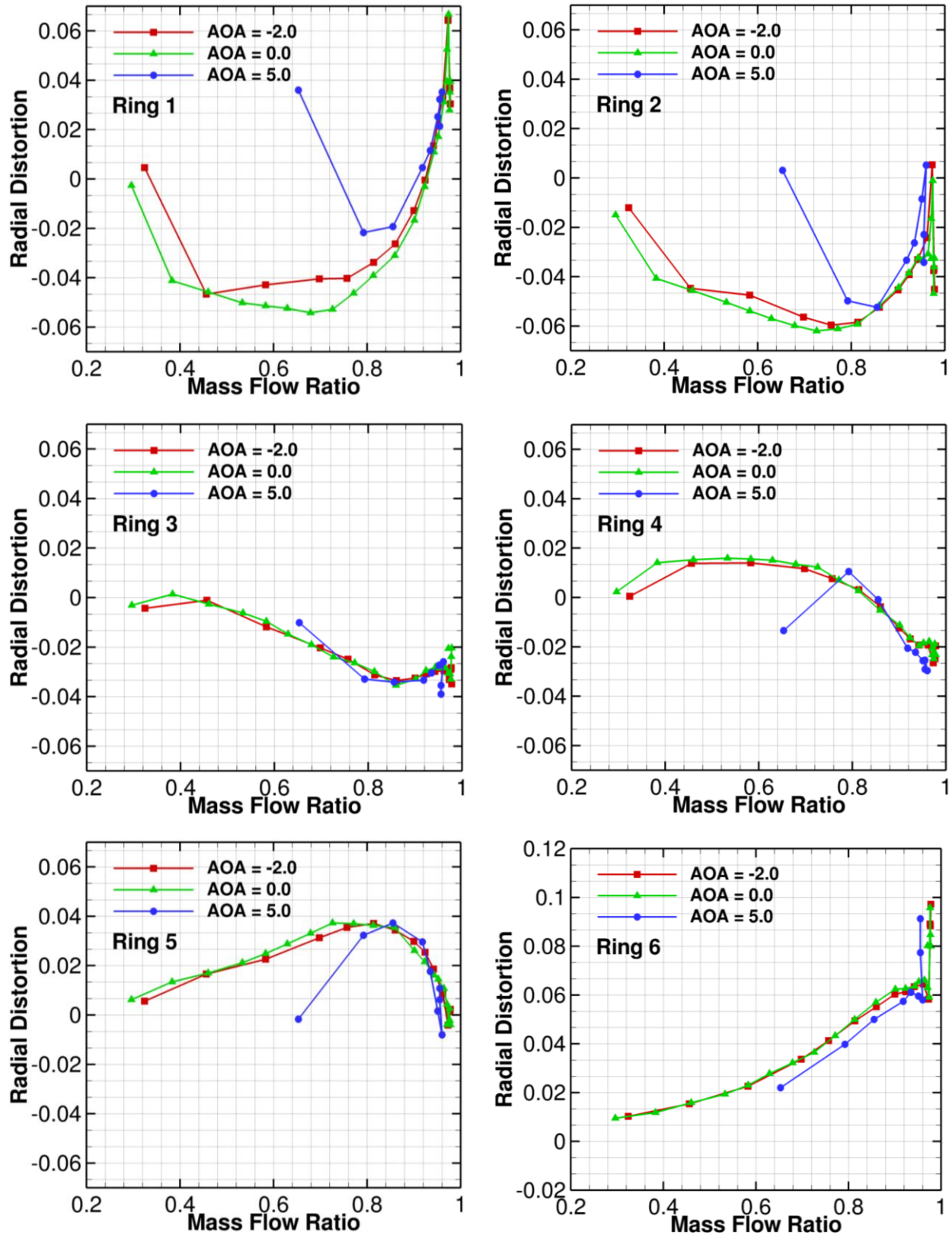


Figure 10: Baseline ring-average radial distortion coefficient

Figure 11 shows a comparison of the normalized velocity profiles at the forward boundary-layer rake at the design point and a point prior to the onset of buzz at varying angles of attack. The normalized velocity is defined as the local velocity divided by the freestream velocity:

$$\text{Normalized Velocity} = \frac{U_{local}}{U_{\infty}} \quad (4)$$

The results show that as the angle of attack increases from -2.0 to 5.0 the boundary layer becomes fuller. At negative angle of attack, as the flow moves past the shoulder in the bottom half of the centerbody it experiences a large turn-angle to follow the centerbody contour as the flow enters the diffuser. As the angle of attack is increased to zero, the flow along the centerbody becomes symmetric and flow experiences the same turn-angle on the top and bottom half of the duct, thus the flow follows the centerbody contour easily. However, at high positive angle of attack the flow experiences large turn-angles on the top half of the centerbody, which means the flow traveling along the bottom half notices small turn-angles and the flow follows the hub side contour better. The trend would reverse if the forward boundary-layer rake was located on the top half of the centerbody for the same angle of attack.

Figure 11 also confirms the absence of flow separation induced by the SBLI upstream of the centerbody shoulder. The upstream micro-VGs were intended to reduce the effects of SBLIs and improve normal shock stability, but the baseline results showed little SBLI effect and no normal shock instability.

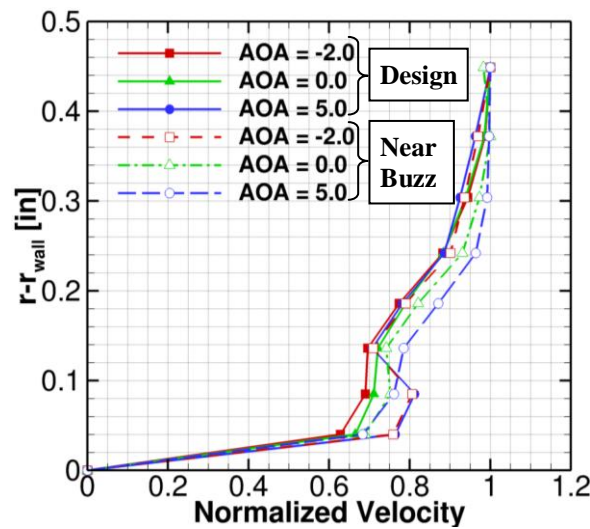


Figure 11: Baseline boundary-layer profile at forward rake

Figure 12 shows a comparison of velocity profiles at the aft boundary-layer rake at the design point and a point prior to buzz at varying angles of attack. The profiles at the design point showed a relatively flat gradient close to the hub; however the profiles prior to onset of buzz showed a steeper gradient close to the hub for -2° and 5° angles of attack. This behavior of boundary-layer thickening was expected as the inlet was throttled. The thickening of the boundary layer can also cause increased levels of flow distortion. The downstream VGs were used with a purpose of reducing the hub side boundary-layer thickening and flow distortion.

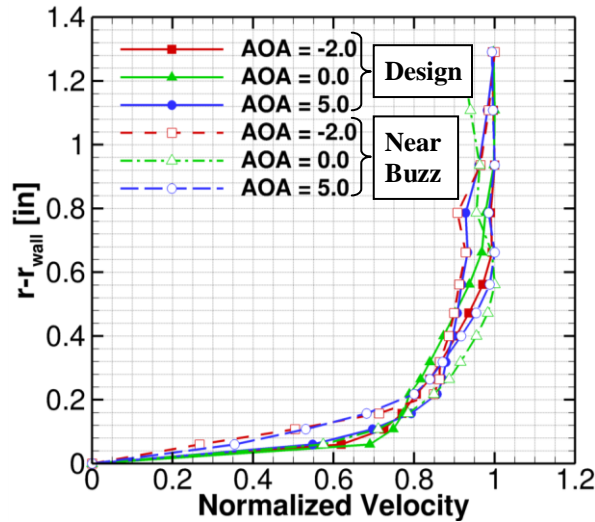


Figure 12: Baseline boundary-layer profiles at aft rake

B. Vortex Generator Configurations

Four upstream micro-VGs and six downstream VGs were investigated with the purpose of evaluating VG effects on the boundary-layer thickness and over all inlet performance. The following discussions focus on the design Mach number 1.7 and 0° angle of attack. The higher angle of attack results are not discussed further for the sake of brevity and to avoid repetition as the trends are similar. The total pressure recovery and AIP flow distortion plots are presented followed by normalized boundary-layer velocity profiles.

The effects of downstream VG configurations on the inlet total pressure recovery shown in Fig. 13-a indicate a subtle difference between VG configurations and a variation in peak recoveries of 0.02. The addition of downstream VG configurations causes a marginal decrease in the peak recovery values relative to the baseline case. Combinations of the upstream micro-VG and the downstream VG configurations, Fig. 13-b, caused no significant change in the peak recovery values. However, the U2R-D4R configuration caused the inlet to buzz sooner and resulted in a reduced buzz margin.

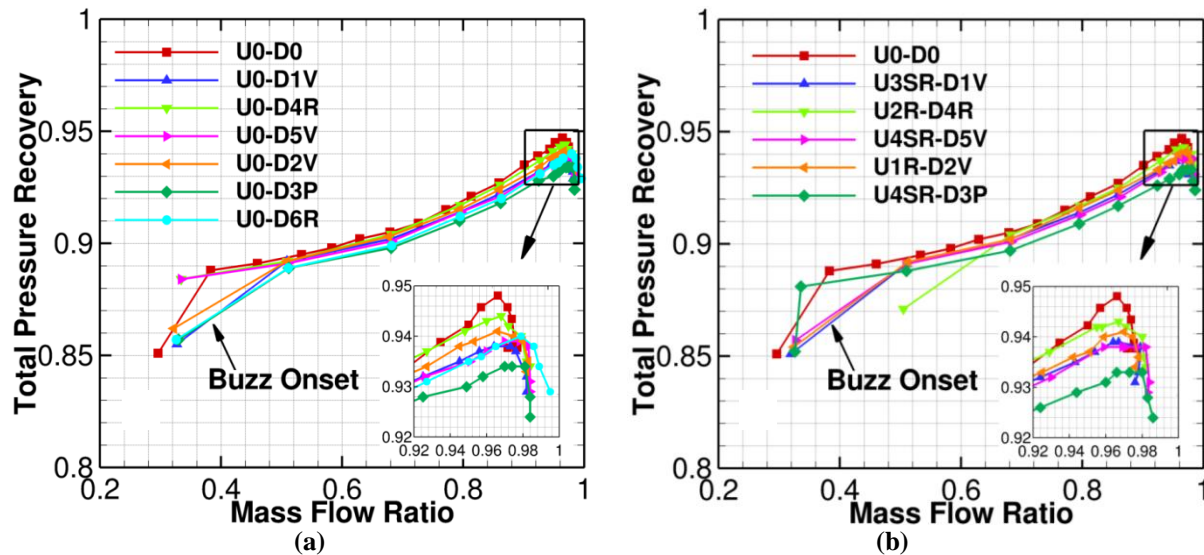


Figure 13: Total pressure recovery for all VG configurations

Figure 14-a shows a comparison of the DC60 flow distortion coefficient, defined in Eq. 1, calculated after placing the downstream VGs on the centerbody. The plow- and ramp-type VGs, D3P and D6R respectively,

produced some of the highest distortion levels. Such high distortion content was a direct effect of the upwash created by the D3P and D6R VGs interacting with the strut wake at the bottom dead center. The circumferential placement of these VGs close to the AIP rake at the bottom dead center allowed the capture of the upwash effect. Other ramp-type VGs did not produce an upwash close to the bottom dead center rake; as a result the calculated DC60 distortion coefficient was lower. It was also interesting to notice that vane-type VGs produced some of the lowest distortion levels. Even though D2V produced an upwash near the bottom dead center, the AIP rake did not measure any significant effect.

A similar trend can be observed in Fig. 14-b, where the upstream micro-VGs were utilized with downstream VGs. The upstream micro-VG effects on the distortion levels were insignificant.

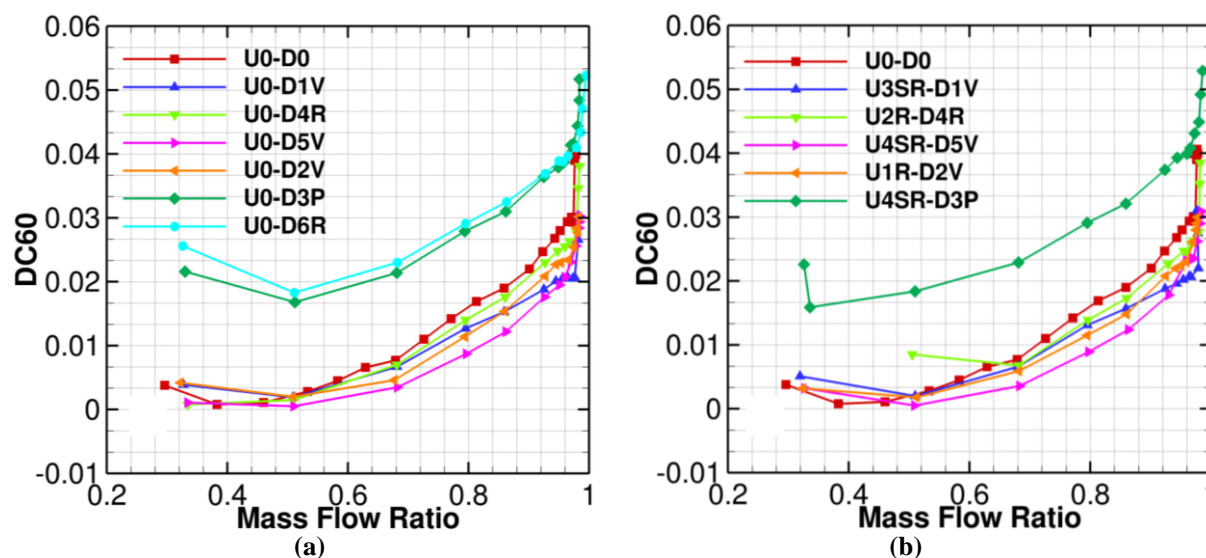


Figure 14: Distortion coefficient for all VG configurations

The ring-average radial distortion coefficient profiles shown in Fig. 15 reveal the distinct behavior of vane-, ramp- and plow-type VGs near the hub. The ring-average distortion for ring two was lower for all downstream VGs when compared to the baseline, see Fig. 15-a. The distortion nearest to the wall showed an apparent difference between the vane-, ramp-, and plow-type VGs. The negative values of distortion for vane-type VGs suggest that the ring-average total pressure was higher than the face-average. In contrast, the ring-averaged total pressure for ramp- and plow-type VGs was lower than the face-average. The vane-type VGs produced a more uniform flow relative to the other VG types, which was obvious from the low flow distortion gradients close to the wall. D2V resulted in the most uniform flow on the hub side; however it produced a higher distortion level than D5V, which produced the lowest distortion levels on rings 1 and 2.

Figure 15-b shows a comparison of both the upstream and downstream VG combinations. Overall, the addition of upstream micro-VGs resulted in higher flow non-uniformity at the hub. The U4SR-D3P combination produced the highest distortion at the hub.

The flow distortion on the tip side (ring 6) was high compared to the hub. This is caused by the normal shock impingement at the cowl tip. The small variation in the flow distortion among VG configurations was due to minor change in the tunnel flow conditions and not a VG effect.

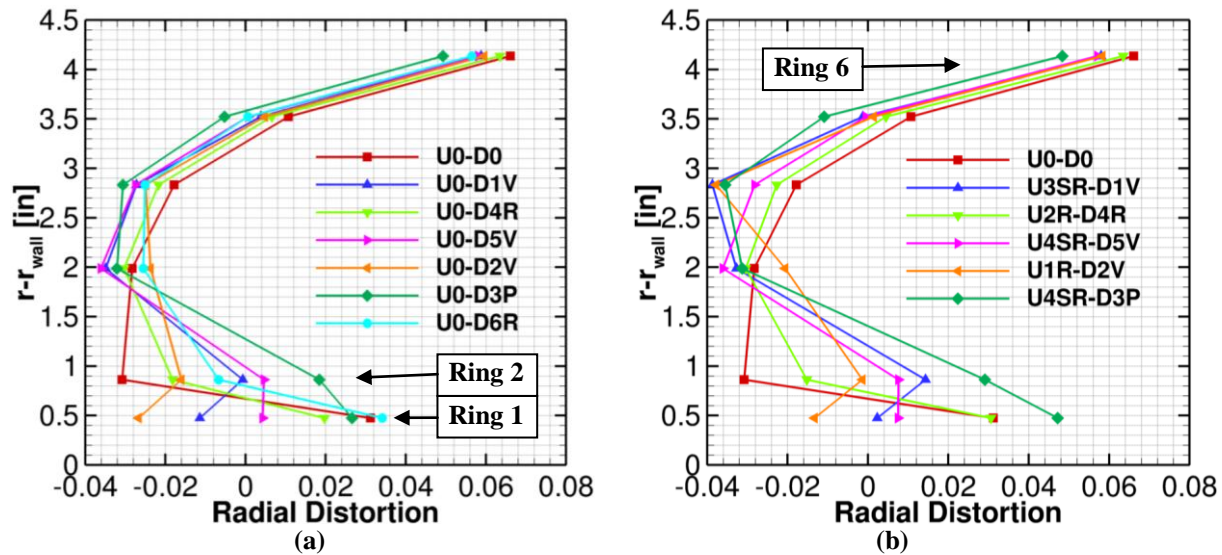


Figure 15: Ring-average radial distortion coefficient profile at design point for all VG configurations

Figure 16-a shows the effect of only downstream VGs on the forward boundary-layer rake velocity profiles at the design point. Except for D6R, all downstream VGs made a noticeable improvement in the boundary-layer thickness. Downstream VG D6R was positioned so that the aft boundary-layer rake was in the downwash plane between the two ramps. Thus, small ramp size and circumferential VG placement did not allow for the aft boundary-layer rake to measure the D6R VG upwash effect. The vane-type VGs (D1V, D2V and D5V) performed better than the ramp- and plow-type VGs, D4R and D3P respectively. The ramp-type VG D6R was the least beneficial of all downstream VGs.

Figure 16-b shows a combined effect of upstream micro-VGs and downstream VGs on the forward boundary-layer rake at the design point. The addition of upstream micro-VGs showed little to no change in the boundary-layer thickness. Thus, the upstream micro-VGs had no significant effect on the shock stability. In the U1R-D2V case the boundary-layer profile deteriorated slightly compared to the D2V only case.

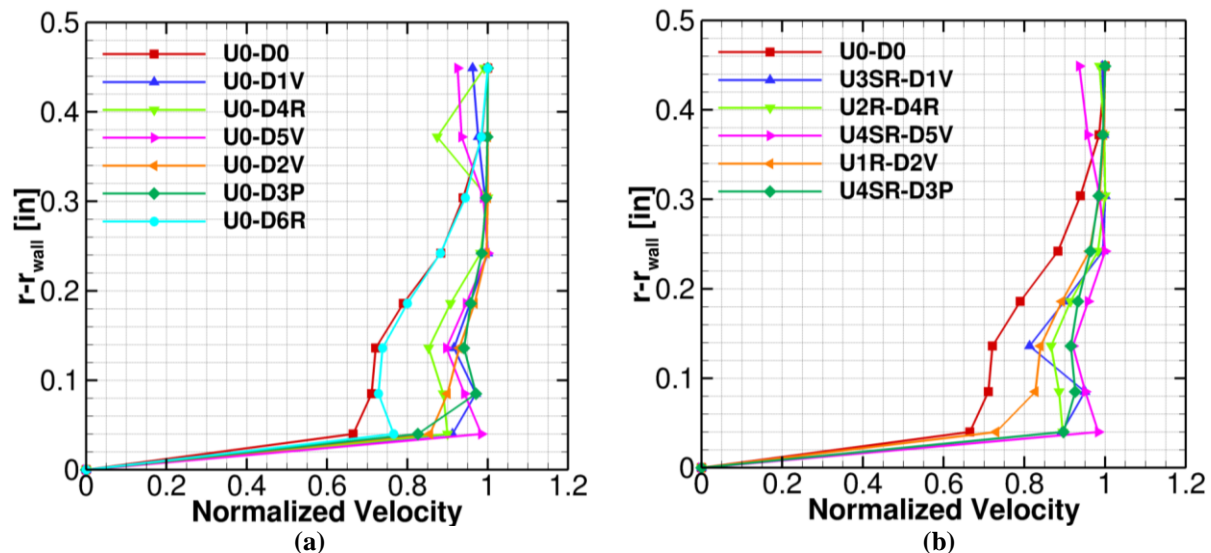


Figure 16: Boundary-layer profile at forward rake at design point for all VG configurations

Figure 17-a shows the effect of only downstream VGs on the aft boundary-layer rake velocity profiles at the design point. The ramp-type VG, D6R caused boundary-layer thickening. Thus, D6R was not chosen for further evaluation. The ramp-type VG, D4R showed a moderate effect on the boundary layer. The downstream VGs D1V, D2V, D5V, and D3P showed the most promise at the aft boundary-layer rake.

In particular, the rake data indicated a momentum deficit away from the wall for the vane-type VG D1V. This deficit results from the transfer of the high momentum flow at the boundary-layer edge to the wall region. The D2V VG is designed similar to D1V but instead has the suction sides of the VGs facing each other. This results in a downwash region which produced a relatively uniform aft rake velocity profile.

Figure 17-b shows a combined effect of the upstream micro-VGs and downstream VGs on the aft boundary-layer rake velocity profiles at the design point. The use of upstream micro-VGs resulted in a slight near wall boundary-layer change. For the U3SR-D1V case, the momentum deficit in the outer portion of the boundary layer increased slightly with the addition of the upstream VGs, while for the remaining cases the near-wall velocity was reduced relative to downstream only VGs.

The downstream VGs help to improve the boundary-layer thickness. As indicated by data from both the forward and aft boundary-layer rakes. Upstream micro-VGs did little to positively impact the boundary layer and often the effects were negative.

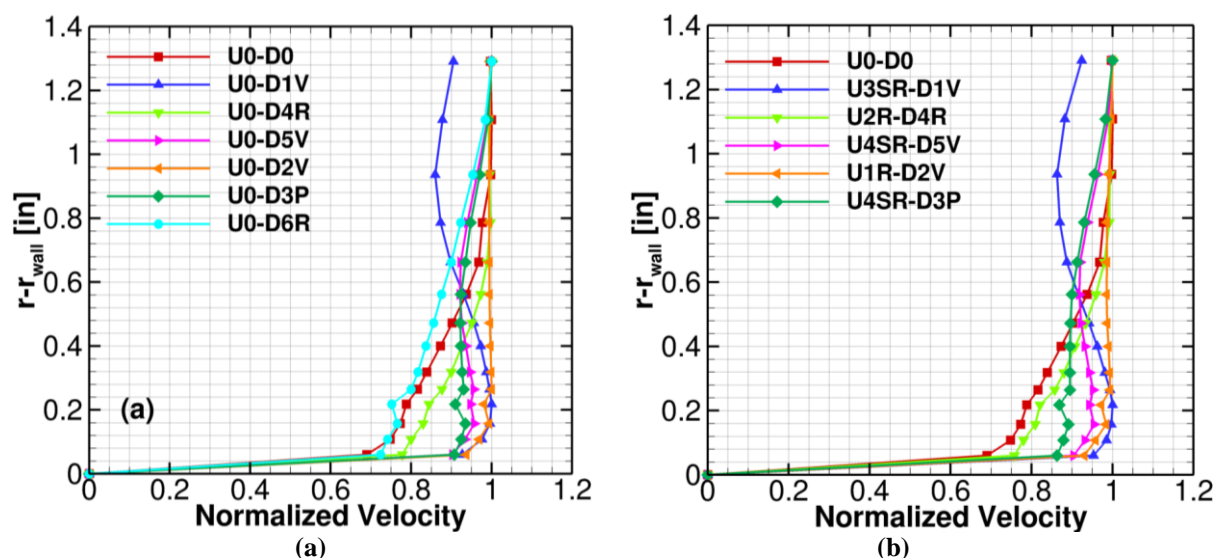


Figure 17: Boundary-layer profile at aft rake (at design point for all VG configurations)

C. AIP Dynamic Pressure Analysis

Of the eight dynamic pressure transducers installed on the AIP rakes (Fig. 6), the focus of this section will be on the ones closest to the centerbody (i.e., the ones influenced most by the VGs). These transducers were located 90° apart and were 0.475 inches from the centerbody surface, making them roughly the same height as the downstream vane-, ramp-, and plow-type (D1V, D2V, D3P, and D4R) VGs. At this height, the transducers were able to measure the direct impact of the VG configurations.

Dynamic pressure data, sampled at 5000 Hz, were collected over a five second period. Data were taken for each test condition and a unique upstream micro-VG and downstream VG configuration. Presentation of the data will be shown as either an average sound pressure level (SPL) at the hub side of the AIP or as a frequency spectrum of relative amplitudes. SPL curves provide a quick means of evaluating quantitative differences in the configurations at changing flow conditions. An alternate means of comparison would be to calculate a dynamic pressure coefficient. However for the limited range of Mach numbers, using the imbedded log scaling in the SPL calculation provides a reasonable method for comparison.

Starting with the baseline (U0-D0) configuration, the hub side dynamic pressure transducer average loudness levels are provided as a function of both mass flow ratio and Mach number in Fig. 18-a. General trends include decreased loudness with decreased mass flow ratio or lower freestream Mach numbers. At the higher mass flow ratios the rapid decrease in loudness with decreasing mass flow ratio occurs as the flow field becomes established on the centerbody, changing from a boundary layer that is thicker to one that is thicker but more unsteady.

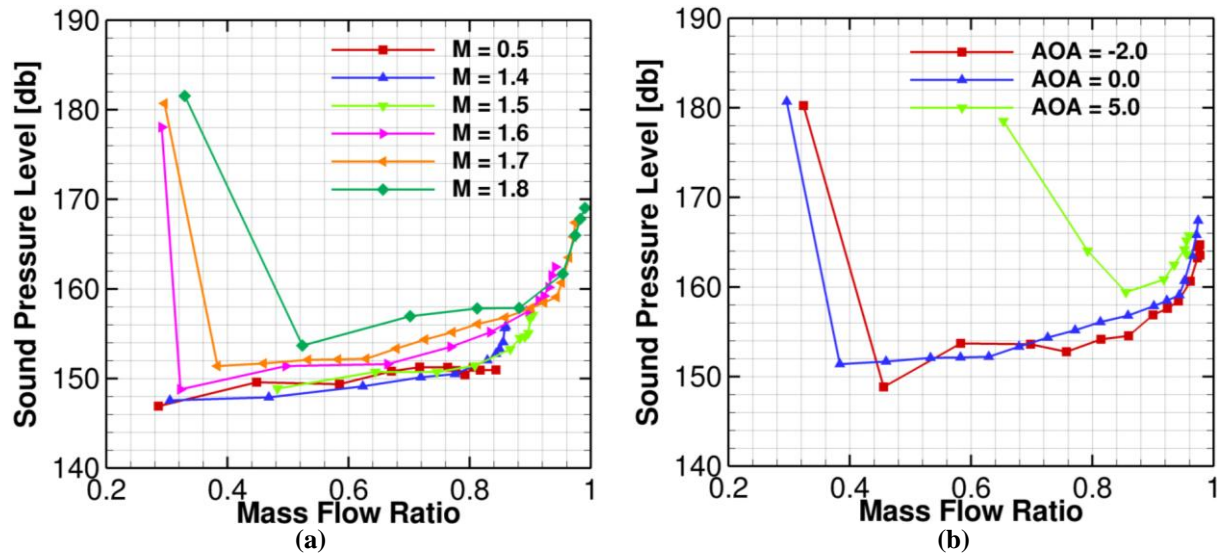


Figure 18: Baseline average sound levels with a) 0° AOA and b) Mach 1.7

The other dominant feature in these plots was the sudden increase in sound pressure level at very low mass flow ratio (<0.5). This was associated with test conditions where the model was placed into buzz. At this condition, the pressure fluctuations were on the order of ± 3 psi. These trends are exhibited for all configurations regardless of the VG arrangements. The impact of angle of attack at a constant Mach number showed increased loudness with increasing angle of attack, which is shown in Fig. 18-b.

A comparison of all VG configurations, shown in Fig. 19, clearly illustrates the benefit of VGs in decreasing AIP hub side loudness. Or put another way, the addition of the VGs created a thinner boundary-layer profile. The largest improvement in the loudness was obtained from the vane-type VGs D1V and D5V. The addition of upstream micro-VGs did not result in additional loudness improvement.

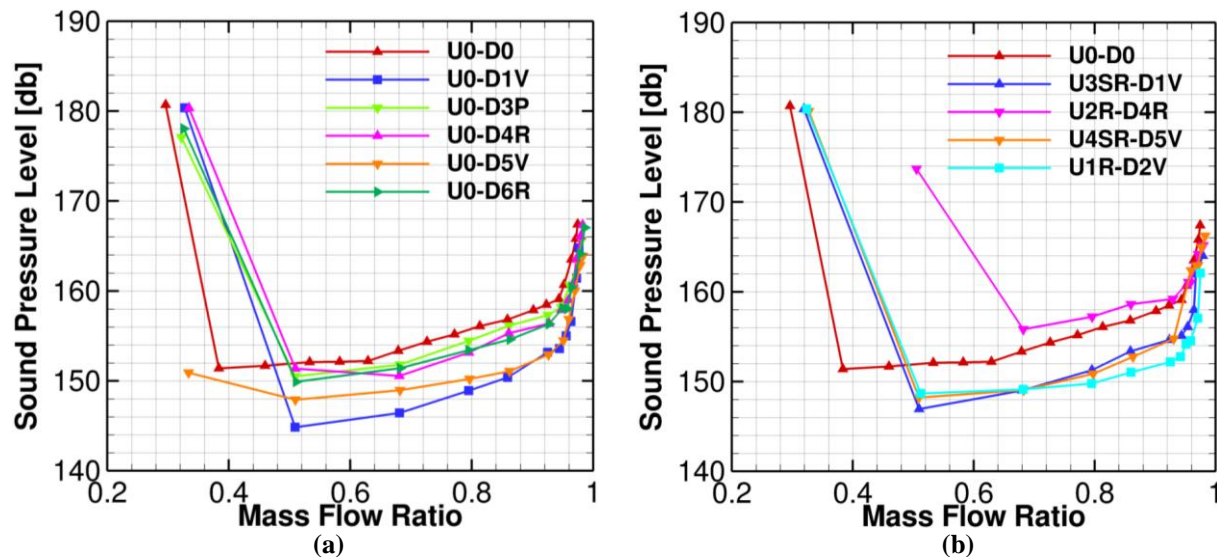


Figure 19: Effect of VG's on average sound levels at Mach 1.7 and 0° angle of attack with a) downstream only VGs and b) both VGs

All of the spectral data presented was done using the dynamic pressure transducer positioned at 90°. This transducer exhibited behavior typical of the other three transducers and was functional over the entire period of testing. This transducer was clear of the primary strut wake influence and provided stable measurements for all the VG configurations tested. Looking at both the signal traces and amplitude spectral plot for the baseline, shown in Fig. 20, it can be seen that much of the loudness (energy) in the flow resides at very low frequencies (<20 Hz) with

reduced amplitudes occurring at frequencies above this threshold. An amplitude spectra plot set is provided in Figs. 21 to 25 for selected VG configurations at the mass flow ratio consistent with design.

Of interest in the amplitude spectra plots is the behavior of the vane-type VGs (D1V, D2V, and D5V) shown in Figs. 21, 22, and 25. For each of these configurations there are a couple of additional features at ~250 and ~310 Hz that have amplitude levels similar to the low frequency feature. They differ from the low frequency feature in that they are time dependent, appearing and disappearing. Configuration U0-D4R, Fig. 23, is also unique in that there is a definite break-up of the low frequency feature when compared to the baseline. However, addition of the upstream micro-VG U2R to D4R results in the return of the low frequency feature.

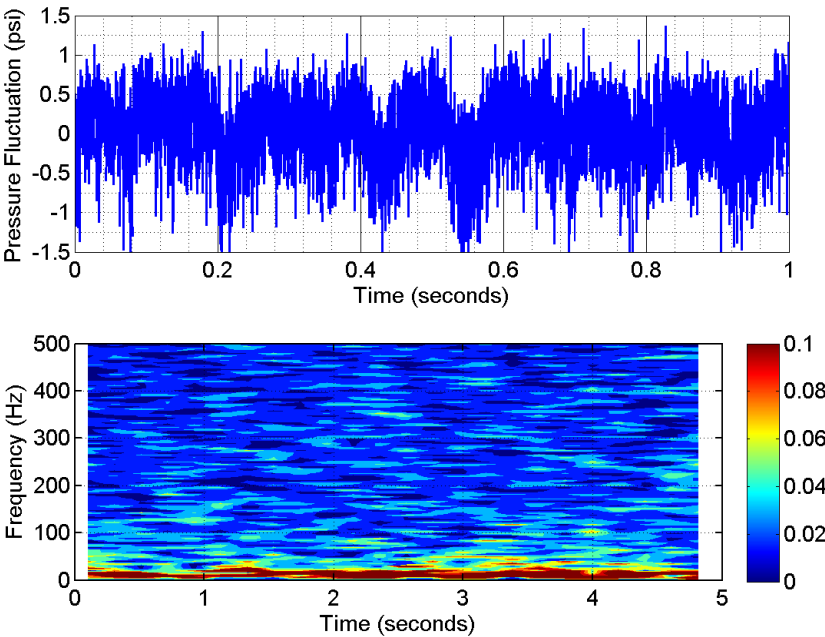


Figure 20: Baseline spectra at Mach 1.7 and 0° angle of attack

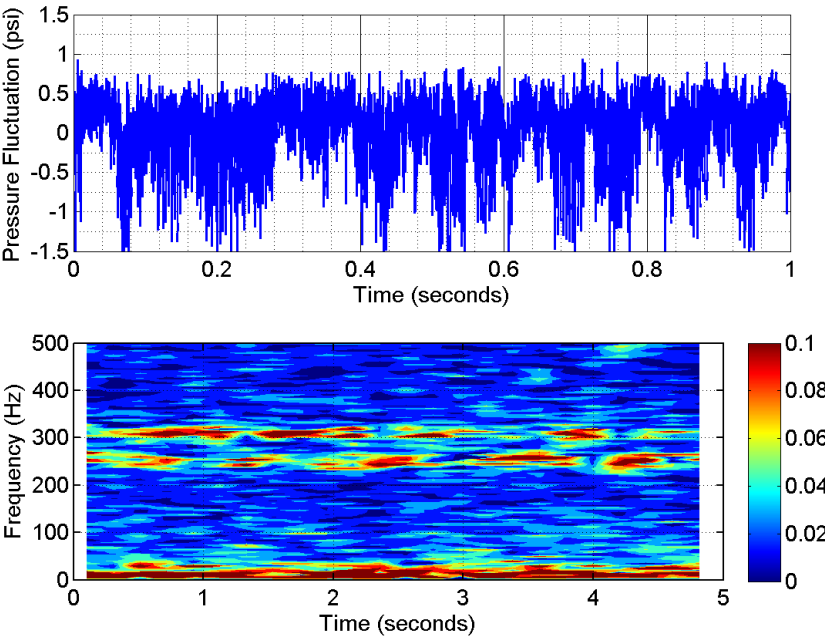


Figure 21: Spectra for U0-D1V at Mach 1.7 and 0° angle of attack for design point

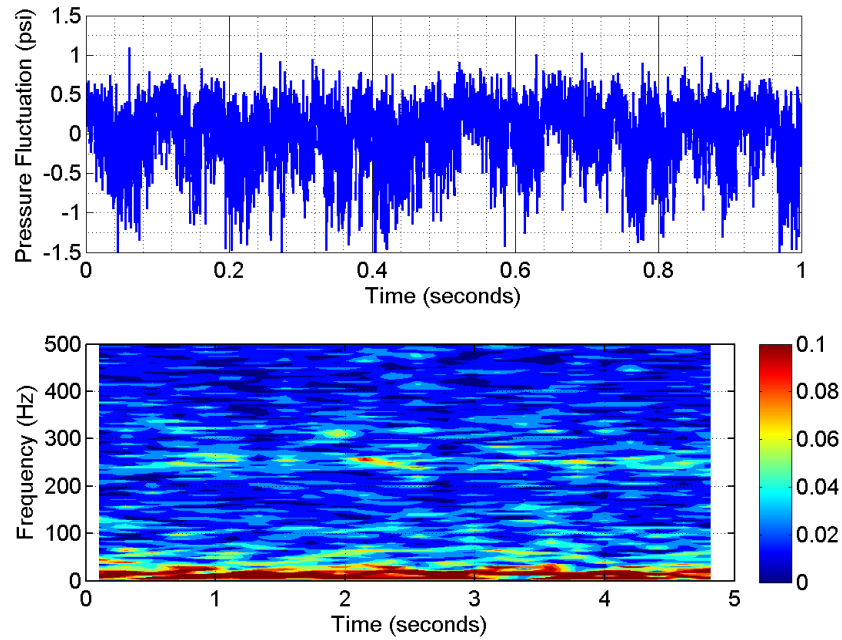


Figure 22: Spectra for U3SR-DIV at Mach 1.7 and 0° angle of attack for design point

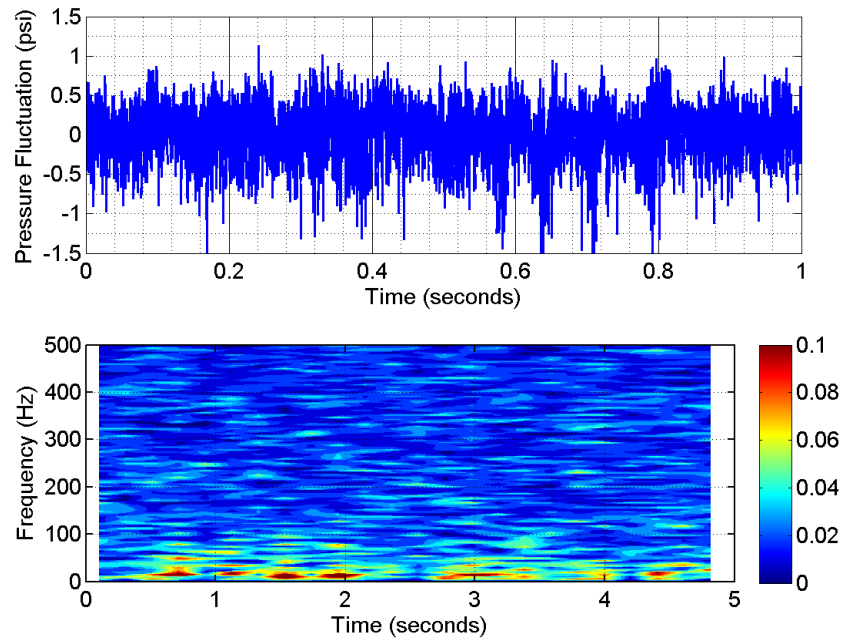


Figure 23: Spectra for U0-D4R at Mach 1.7 and 0° angle of attack for design point

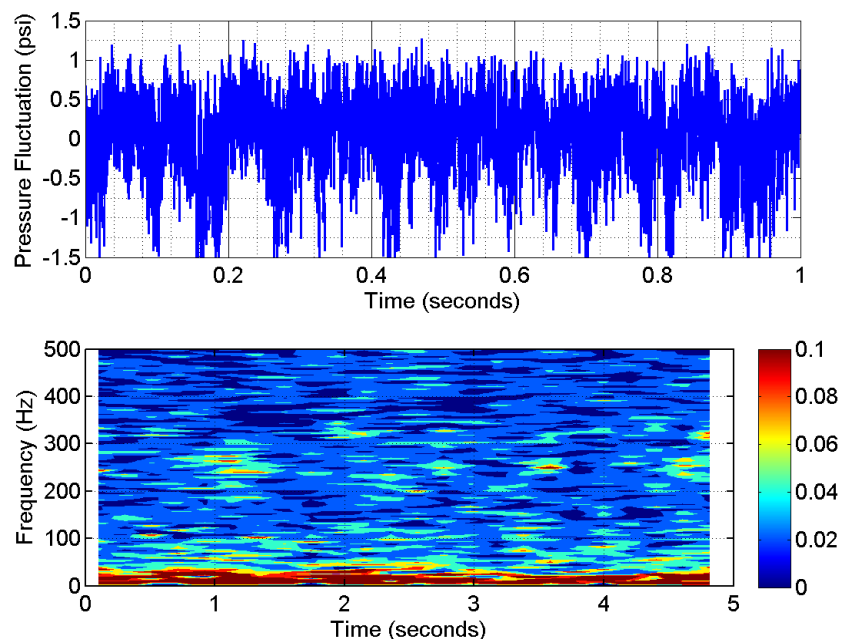


Figure 24: Spectra for U2R-D4R at Mach 1.7 and 0° angle of attack for design point

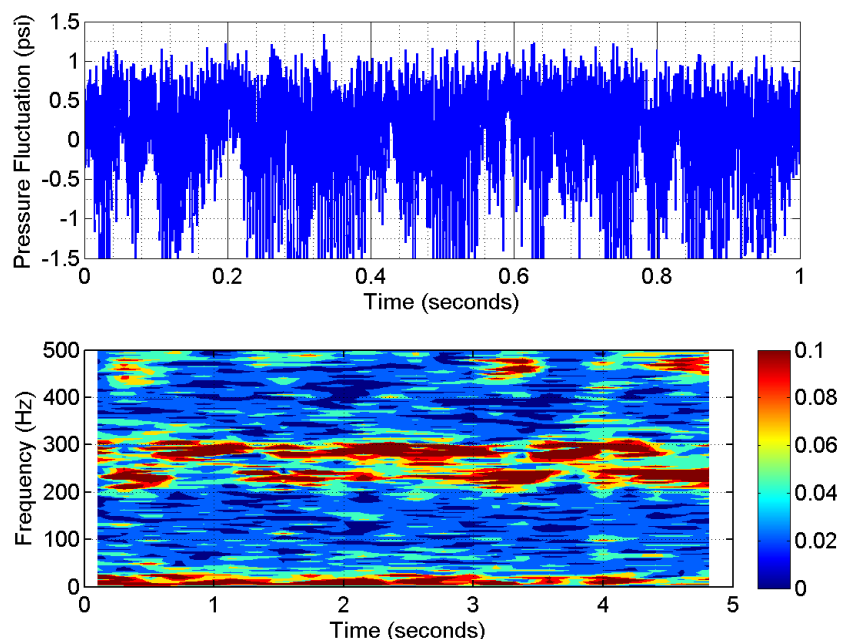


Figure 25: Spectra for U0-D5V at Mach 1.7 and 0° angle of attack for design point

IV. Conclusions

Vortex Generators (VGs) were experimentally investigated on a single-stream Low-Boom Supersonic Inlet. VGs were placed upstream of the throat normal shock for shock stability and to reduce boundary-layer thickness on the inlet centerbody. The downstream VGs were placed aft of the shock to reduce the boundary-layer thickness and flow distortion. Four upstream micro-VGs and six downstream VGs were designed and fabricated for this purpose.

The results presented in this paper show that the upstream micro-VGs had no significant positive effect on the hub side boundary layer. Although, the shock boundary-layer interactions never caused a separation, thickening of the boundary layer was observed at high angles of attack. The boundary layer was measured by a forward and aft boundary-layer rake. The forward rake was located just aft of the centerbody shoulder and downstream VGs. The aft

rake was located at the same axial station as the AIP rakes. The upstream micro-VGs showed a subtle effect when comparing the boundary-layer velocity profiles, inlet recovery curves and DC60 distortion coefficient. However, the ring-average distortion showed isolated effects of the upstream micro-VGs, but the magnitude of the impact was small.

In contrast, the downstream VGs demonstrated a significant improvement in the hub side boundary layer. However, the inlet total pressure recovery decreased marginally. The largest drop in the inlet peak recovery was 0.02. The DC60 distortion coefficient showed a definite reduction with the downstream VGs except for the plow-type and small ramp-type VGs. The vane-type VGs produced some of the lowest distortion levels.

The dynamic pressure analysis showed that the sound pressure levels increased with an increase in the angle of attack. Addition of VGs showed a distinct reduction in the sound pressure levels as well as a thinner boundary-layer at the hub. The spectra plots showed that the loudness or the energy in the flow resides at very low frequencies (<20 Hz). Time dependent frequencies at approximately 250 and 310 Hz were also observed for only vane-type VGs. Only the large ramp-type VG showed the break-up of the high amplitude spectra at low frequency which was common in all configurations. The vane-type VG that produced a downwash showed a similar effect but not as effective as large ramp-type VG.

In summary, the use of VGs, especially the downstream VGs, showed a reduction in the hub-side boundary-layer thickness. It produced fuller and more uniform velocity profiles, lower distortion and sound pressure levels.

Acknowledgments

The authors would like to acknowledge the support of the broad team that made this work possible: specifically, researchers at the University of Illinois Urbana-Champaign, University of Virginia, and Gulfstream Aerospace Corporation, the model work by TriModels, and the facility team at the 8x6 foot Supersonic Wind Tunnel at NASA GRC. The Supersonics Project of the NASA Fundamental Aeronautics Program supported this work.

References

- ¹Tilman, C. P., Kimmel, R. G., Addington, G. A., and Myatt, J. H., "Flow Control Research and Applications at the AFRL's Air Vehicle Directorate," AIAA-2004-2622, 2004.
- ²Van Wie, D. M., and Nedungadi, A., "Plasma Aerodynamic Flow Control for Hypersonic Inlets," AIAA-2004-4129, 2004.
- ³Hirt, S. M., and Anderson, B. H., "Experimental Investigation of the Application of Microramp Flow Control to an Oblique Shock Interaction," AIAA-2009-919, 2009.
- ⁴Allan, B. G., and Owens, L. R., "Numerical Modeling of Flow Control in a Boundary-Layer-Ingesting Offset Inlet Diffuser at Transonic Mach Numbers," AIAA-2006-845, 2006.
- ⁵Vyas, M. A., Hirt, S. M., and Anderson, B. H., "Experimental Investigation of Normal Shock Boundary-Layer Interaction with Hybrid Flow Control," 29th AIAA Applied Aerodynamics Conference, 2011 (submitted for publication).
- ⁶Hirt, S. M., Chima, R. V., Vyas, M. A., Wayman, T. R., Conners, T. R., and Reger, R. W., "Experimental Investigation of a Large-Scale Low-Boom Inlet concept," 29th AIAA Applied Aerodynamics Conference, 2011 (submitted for publication).
- ⁷Chima, R. V., Hirt, S. M., and Reger, R. W., "Axisymmetric calculations of a Low-Boom Inlet in a Supersonic Wind Tunnel," 29th AIAA Applied Aerodynamics Conference, 2011 (submitted for publication).
- ⁸Conners, T. R., and Howe, D. C., "Supersonic Inlet Shaping for Dramatic Reductions in Drag and Sonic Boom Strength," AIAA-2006-30, 2006.
- ⁹Conners, T. R., and Wayman, T. R., "The Feasibility of High-Flow Nacelle Bypass for Low Sonic Boom Propulsion System Design," 29th AIAA Applied Aerodynamics Conference, 2011 (submitted for publication).
- ¹⁰Seddon, J., and Goldsmith, E. L., *Intake Aerodynamics*, AIAA Education Series, AIAA, New York, 1985.
- ¹¹Trapier, S., Duveau, P., and Deck, S., "Experimental Study of Supersonic Inlet Buzz," AIAA Journal, Vol. 44, No. 10, 2006.
- ¹²"Gas Turbine Engine Inlet Flow Distortion Guidelines," Aerospace Recommended Practice, SAE International, ARP1420, Rev. B, 2002.